PROGRAMMED MATERIALS

Stretchable surfaces with programmable 3D texture morphing for synthetic camouflaging skins

J. H. Pikul,[1,2] S. Li,[3] H. Bai,[1] R. T. Hanlon,[4] I. Cohen,[2] R. F. Shepherd[1,3]*

Technologies that use stretchable materials are increasingly important, yet we are unable to control how they stretch with much more sophistication than inflating balloons. Nature, however, demonstrates remarkable control of stretchable surfaces; for example, cephalopods can project hierarchical structures from their skin in milliseconds for a wide range of textural camouflage. Inspired by cephalopod muscular morphology, we developed synthetic tissue groupings that allowed programmable transformation of two-dimensional (2D) stretchable surfaces into target 3D shapes. The synthetic tissue groupings consisted of elastomeric membranes embedded with inextensible textile mesh that inflated to within 10% of their target shapes by using a simple fabrication method and modeling approach. These stretchable surfaces transform from flat sheets to 3D textures that imitate natural stone and plant shapes and camouflage into their background environments.

Numerous living organisms, ranging from flowers to marine invertebrates such as cephalopods, use soft tissue to reversibly change shape for camouflage, locomotion, grasping, and moving objects (*1*–*6*). Inspired by these capabilities, scientists and engineers have demonstrated pioneering examples of locomotion and object manipulation in soft materials by controlling nonsymmetric volume changes in compliant appendages (*7*–*11*). Achieving nonsymmetric hierarchical surfaces required for camouflage, however, is more challenging because it is necessary to design and control the transformation of two-dimensional (2D) planar surfaces into complex 3D non-Euclidean shapes. Although there are several candidate technologies that enable the control of soft material surfaces [hydrogels (*12*–*16*), shape-memory polymers (*17*, *18*), and liquid crystal elastomers (*19*), among others (*20*–*23*)], pneumatic actuation of stretchable elastomers is particularly appealing because of fast actuation rates [frequency (*f*) ~ 4 Hz] (*24*), the ability to be cycled millions of times (*24*), high energy density (~80 J g^{-1} for compressed air) (*25*), and scalable manufacturing over millimeter- to meter-length scales (*24*, *26*). Designing the shape of inflated elastomeric surfaces, however, has been a challenge because of their nonlinear mechanics, large number of configurations that a surface can deform to, and lack of computationally efficient models that can predict the final shape (*27*–*31*).

We took initial inspiration from the form and function of cephalopod papillae (*4*–*6*). The erector muscle fibers in a conical cephalopod papilla extend horizontally across the diameter of a papilla's apex and in concentric circular patterns in a papilla's main axis. Contraction of these erector muscles creates a force toward the papilla's central axis, which pressurizes and stretches (in tension) the connecting soft tissue in a direction normal to the skin surface. This muscle geometry enables cephalopods to routinely transform planar, stretchable skin into a continuum of expandable hierarchical 3D shapes of many forms (from flat to

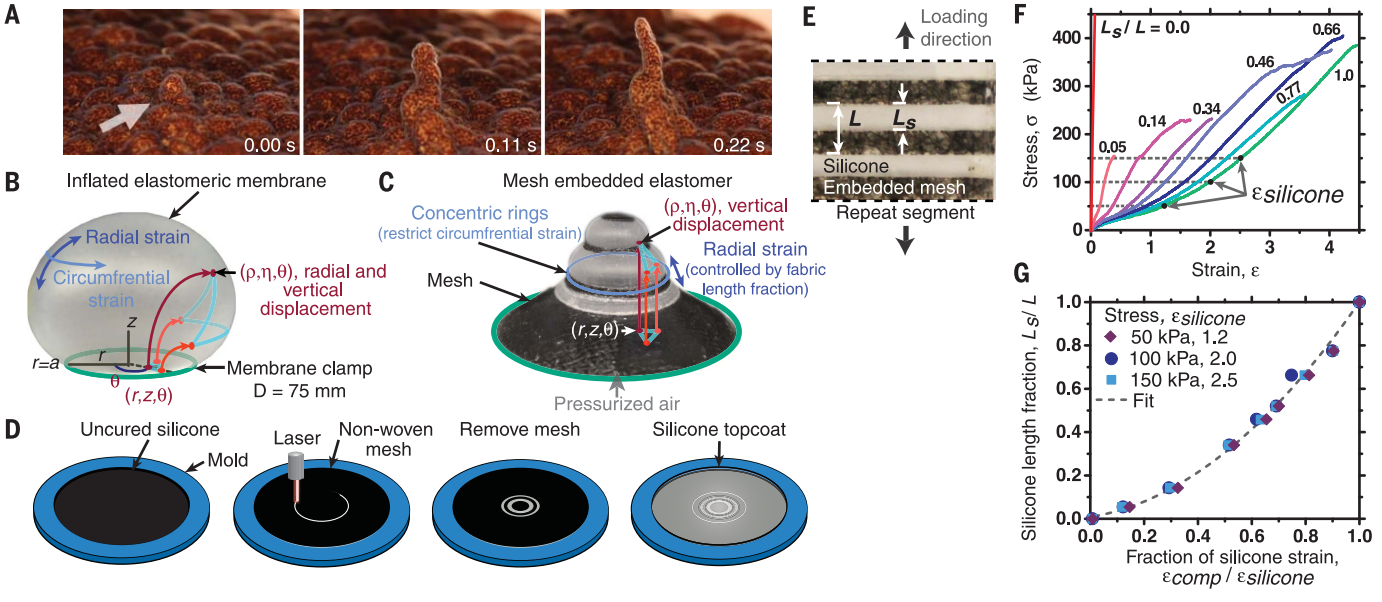

Fig. 1. Inspiration for and description of CCOARSE. (**A**) A conical papilla (~4 mm high) in *Octopus rubescens* that dynamically extends or retracts in ~220 ms. This small species has numerous skin papillae that provide exceptional camouflage in shallow kelp habitats in central California. Frame grabs are from video of a live animal [video: R. Hanlon]. (**B**) An inflated silicone membrane showing the principal strains and resulting deformation of points on the undeformed planar membrane. The radial and circumferential strains displace the points vertically (*v*) and radially (*r*) , but not along θ. (**C**) An inextensible nonwoven mesh embedded in the silicone membrane constrains the circumferential strain, resulting in vertical displacement based on the radial strain. (**D**) Fabrication of the mesh-silicone membrane. Silicone is poured into a mold. Mesh is embedded, laser cut, and removed, and then the silicone is cured. A topcoat of silicone is added to fill voids and improve mesh adhesion. (**E**) A tenstile testing specimen section with horizontal layers of mesh and L_S/L silicone length fraction. (**F**) Stress-strain measurements for specimens with multiple silicone length fractions. (**G**) Relationship between the composite membrane strain and silicone length fraction taken from (F) at 50-, 100-, and 150-kPa membrane stress states. This information maps the mesh design in a silicone-mesh composite membrane to a target 3D shape.

fully extended, and any state in between at ~1 Hz) that dynamically camouflage the cephalopod into their environments [Fig. 1A and movie S1 (copyright Roger Hanlon 2012)]. This basic architecture—known as a muscular hydrostat—relies on incompressible muscle. A cephalopod can create complex 3D papillae shapes (such as vertically flat or trilobed) by arranging the muscles in different orientations and by constructing papillae that have multiple muscular hydrostats working as a unit. By using artificial tissue groupings, inspired by the morphology and mechanical function of cephalopod erector muscles, we developed a one-to-one mapping for reversibly transforming synthetic skins into complex hierarchical shapes. In the end, our material and use of pneumatic actuation also shares mechanical analogies with the fibrous mesh of echinoderm tube feet and the pressurized membrane of the cuticle of a molting crab shell, which assumes a complex 3D shape upon inflation (*32*, *33*).

We used two materials to act as synthetic tissue groupings: a fiber mesh embedded in a silicone elastomer. The fiber mesh acts as local connective tissue fiber reinforcement that, similar to erector muscles in papilla, provides a force toward the synthetic papilla's central axis and controls the 3D shape, while the elastomer acts as stretchable connected tissue that stretches (in tension) normal to the synthetic skin surface, similar to the connecting soft tissue in papillae. We used this binary system to solve the design challenge of mapping a 2D surface into a 3D shape. In the same way that a string wrapped around a balloon will alter its inflated shape, embedding mesh into an elastomeric disk restricts local stretching and prescribes its inflated shape. We patterned inextensible yet flexible mesh in concentric rings so as to constrain the circumferential stretch of the silicone membrane to near zero. This constraint allows a one-to-one mapping from the radial stretch of the elastomer to the target 3D shape displacement, a mechanism we call Circumferentially Constrained and Radially Stretched Elastomer (CCOARSE). The resulting shapes, like cephalopod papillae, can be dynamically inflated to any state between flat and fully erect at frequencies up to 1 Hz.

The CCOARSE mechanism allows for the easy design of complex shapes by relating the radial and circumferential strain distribution in an elastomeric membrane to the target 3D shape (Fig. 1). These strains are denoted by ε_r and ε_c and are defined as

$$\varepsilon_r = \left(\frac{\frac{d\rho^2}{dr} + \frac{d\eta^2}{dr}}{1 + \frac{dz^2}{dr}}\right)^{1/2} - 1 \qquad (1)$$

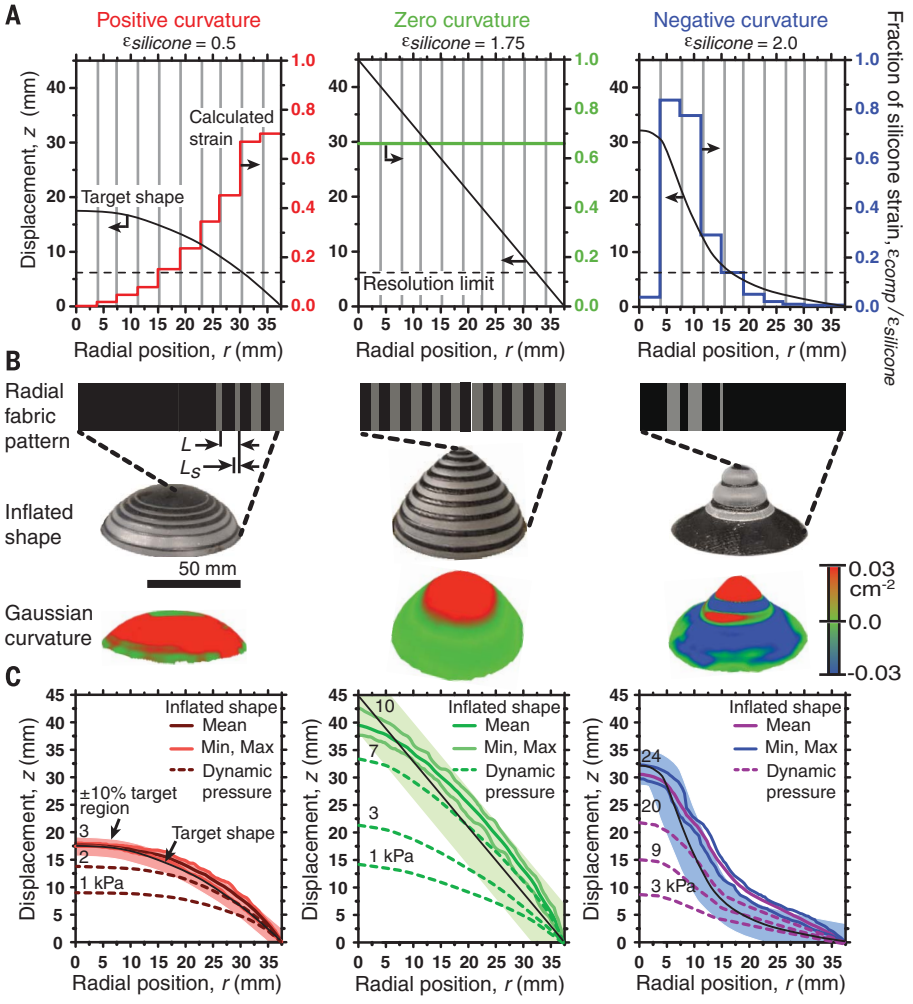

Fig. 2. Design and displacement of axisymmetric membranes with positive, zero, and negative Gaussian curvature target shapes. (**A**) The target shape displacement and composite radial strain versus radial position required to achieve that shape, discretized into 10 segments. (**B**) The radial mesh patterns mapped from the composite radial strain. Black represents mesh, and gray is silicone. *L* is the length between vertical gray lines in (A). The resulting inflated shapes and Gaussian curvatures are shown below the mesh patterns. (**C**) The axisymmetric side profile of the inflated membranes. The solid colored lines are the mean, minimum, and maximum displacement of eight samples tested for each curvature. The highlighted regions behind the target shapes are displacements within 10% of the target shape (solid black line). The dashed lines show the dynamic range of shapes for a representative sample inflated at decreasing pressures.

$$\varepsilon_c = \frac{\rho}{r} - 1 \qquad (2)$$

where the coordinate (r, z) is a point on the undeformed axisymmetric membrane defined in cylindrical coordinates, and (ρ, η) is the location of the same point after the sheet is deformed (*34*). This formulation is illustrated in Fig. 1B through the displacement of three points on a silicone (hyperelastic) membrane clamped to a rigid ring with inner radius a = 37.5 mm and loaded with a uniform pressure. To simplify the design challenge of constructing a strain field given a desired final shape, we set the undeformed membrane to a plane sheet [$z(r)$ = 0] and constrained the deformation so that there was no circumferential strain ($\rho = r$), then

$$\varepsilon_r = \left(1 + \frac{d\eta^2}{dr}\right)^{1/2} - 1 \qquad (3)$$

and ε_c = 0. Under these constraints, the radial strain is directly related to the slope of the membrane in the radial direction ($d\eta/dr$). Because the CCOARSE mechanism is derived from the definition of strain and does not require material properties, it is material independent and therefore broadly applicable as long as the materials used can achieve the required strain (*35*).

[1]Department of Mechanical and Aerospace Engineering, Cornell University, Ithaca, NY 14853, USA. [2]Department of Physics, Cornell University, Ithaca, NY 14853, USA. [3]Department of Materials Science and Engineering, Cornell University, Ithaca, NY 14853, USA. [4]Marine Biological Laboratory, Woods Hole, MA 02543, USA.
***Corresponding author. Email: rfs247@cornell.edu**

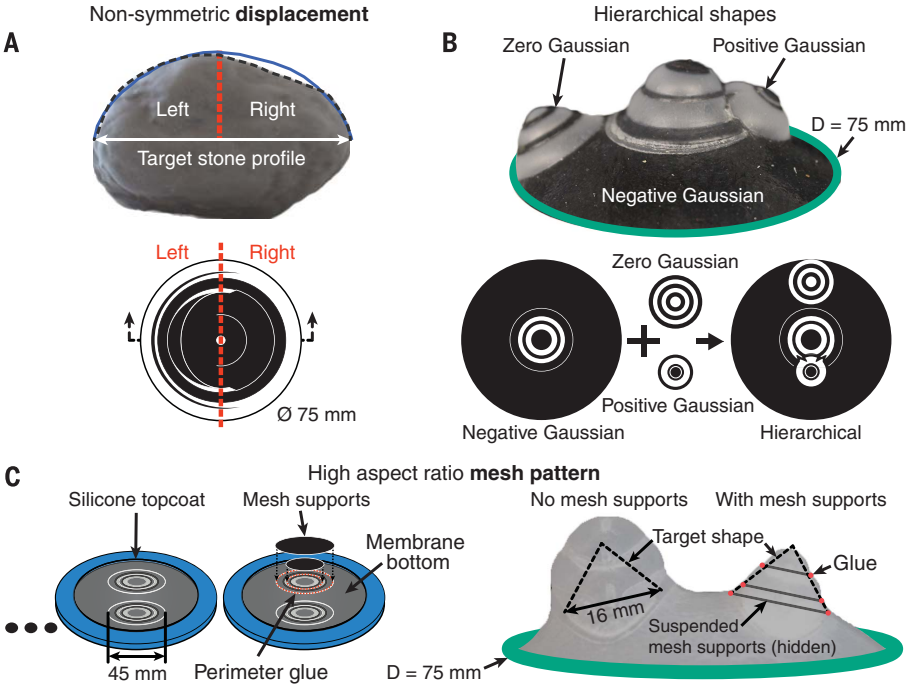

Fig. 3. Design and displacement of membranes with nonsymmetric and hierarchical target shapes. (**A**) A membrane with nonsymmetric target displacement (blue line) designed after a river stone silhouette (dashed line). (**B**) An inflated membrane with second-order hierarchy that combines negative, zero, and positive Gaussian curvature surfaces. (**C**) Adding suspended mesh supports to the membrane underside improves the shape fidelity of high-aspect-ratio mesh patterns by preventing bending of the individual mesh strips. The inflated membrane has two elliptical membranes with 16 mm initial width across the minor axis. The right membrane has suspended mesh supports.

We demonstrated the CCOARSE mechanism in pneumatically actuated membranes composed of low elastic modulus, E ~ 38 kPa at $\varepsilon = 1$, silicone (Ecoflex 00-30, Smooth-On) embedded with concentric rings of high elastic modulus, E ~ 7.7 MPa, nonwoven mesh (Soft 'n Sheer Stabilizer, Sulky) that resists stretching. The concentric mesh rings prevented circumferential strain and restricted the elastomeric membrane to vertical displacement. An example of a silicone-mesh composite membrane pressurized with air (ΔP = 20 kPa) is shown in Fig. 1C, demonstrating high strain in the elastomeric regions and near zero strain in the mesh-patterned areas (movie S2).

In our devices, the spacing between parallel mesh lines determined the local strain in the radial direction and produced an effective, continuous slope much like hatching produces tone or shading in drawing. By using pneumatic actuation, we were able to rapidly cycle (f ~ 1 Hz) texture morphing using a one-to-one mapping from a 2D sheet design to a 3D target shape (movie S3). The tough and resilient elastomers we used allowed for the reversible deformation over hundreds of cycles (*24*). The out-of-plane compliance, isotropic mechanical properties, strength, and porosity of the nonwoven mesh ensured a strong physical bond with the silicone and, despite the large discrepancy in elastic moduli between elastomer and mesh, resulted in smooth shapes with homogenous strain.

The fabrication process we used is simple (Fig. 1C). We first poured silicone into a 3D-printed mold to set the membrane shape and thickness. We then placed nonwoven mesh into the uncured silicone and patterned the mesh using a laser cutter (Zing 24, Epilog). After removing the excess mesh material, we allowed the silicone to cure at room temperature and then poured a final coating of silicone on top. Laser cutting allowed scalable fabrication with 200-μm feature resolution over square-meter areas. Additional fabrication details can be found in the supplementary materials.

To measure the effect of patterning extensible silicone with inextensible mesh, we performed tensile mechanical testing (z010, Zwick/Roell) of 7- by 2-cm samples made from silicone embedded with horizontal mesh strips. A sample segment loaded in the vertical direction is shown in Fig. 1E. We used L_S/L, where L_S is the silicone length and L is segment length, to denote the fraction of silicone not covered by mesh, with $L_S/L = 0$ denoting all mesh and $L_S/L = 1$ denoting no mesh. As the silicone length fraction increased from 0 to 1, the maximum elongation and yield stress increased (Fig. 1F). Composite samples typically failed at the mesh-silicone interface because of the increase in defect sites and increased silicone porosity.

To properly map a target 3D shape using our composite mesh, we determined the relationship between mesh coverage, L_S/L, and the silicone-mesh composite strain relative to pure silicone, $\varepsilon_{comp}/\varepsilon_{silicone}$, at σ = 50, 100, and 150 kPa (Fig. 1F). A single curve, $y = 0.77x^2 + 0.23x$, provided a direct mapping from a target strain to a silicone length fraction on an undeformed membrane. Using Eq. 3, we wrote a Matlab script that traced the outline of a 3D object and calculated the radial strain distribution at each radial coordinate. Using the curve fit in Fig. 1F, this radial strain was converted to 2D silicone length fractions, L_S/L, that guided the inflated membrane to a target shape.

We demonstrated the accuracy of CCOARSE by programing axisymmetric membranes that inflated into 3D positive, zero, and negative Gaussian curvature shapes (Fig. 2). For each target curvature, we divided the radial position r into 10 segments so as to approximate the shape and calculated $\varepsilon_{comp}/\varepsilon_{silicone}$ versus r for each segment (Fig. 2A). The number of radial segments is not an inherent limitation of CCOARSE but indicative of the ~200-μm laser cutter resolution. The radial mesh patterns we embedded into the silicone membranes were mapped from each $\varepsilon_{comp}/\varepsilon_{silicone}$ segment and are shown in Fig. 2B. The mean, minimum, and maximum displacements of eight membranes tested for each Gaussian curvature shape are shown in Fig. 2C. Reducing the input pressure allowed dynamic access to a continuum of shapes between flat and the fully erect target shape (Fig. 2C, dashed curves). Cephalopods use dynamic access to the continuum of shapes between flat and erect in their papilla to successfully adapt their camouflage to a wide variety of environments (*4*–*6*). We found that even with only 10 segments, our CCOARSE approximations are remarkably effective, and the inflated shapes and measured Gaussian curvatures show only small aberrations, on the order of 10% of the target height.

We used CCOARSE to reconstruct natural shapes with nonsymmetric displacements and large variations in slope. We demonstrated this concept on a circular membrane with a single r-z cross section programmed to a nonsymmetric target displacement defined by a stone we found in a nearby river (Fig. 3A, dashed curve). To achieve the nonsymmetric displacement, we embedded the membrane with an axially asymmetric mesh pattern. We used large silicone length fractions on the edges and a nearly continuous mesh near the membrane center to achieve the large variation in angles, 0° to 60°, required for slopes between $0 < d\eta/dr < 2$. The inflated membrane had good shape fidelity in the high-sloped regions and slight deviations in the shallow sloped region where the laser cutter limited the pattern resolution.

To imitate the hierarchical muscle grouping in a cephalopod papilla that allow papillae to access complex shapes, we patterned an inflatable silicone membrane with hierarchical mesh patterns (Fig. 3B and movie S4) (*4*, *5*). Hierarchical

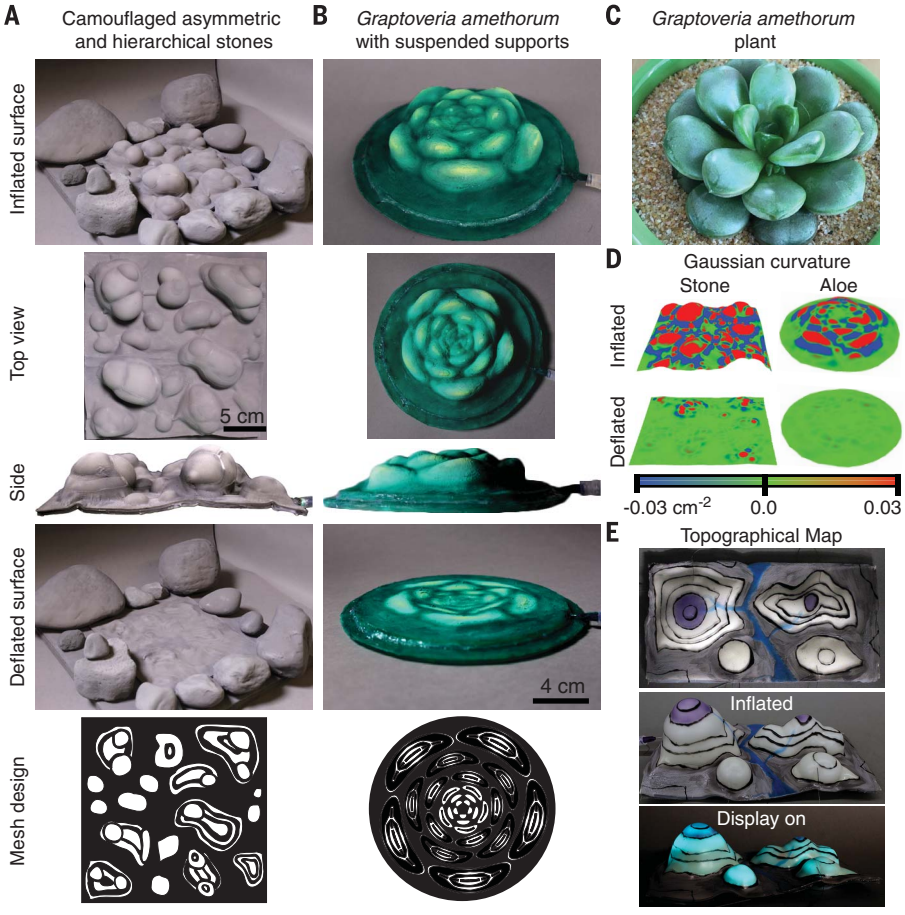

Fig. 4. Membranes programmed to deform into biomimetic shapes by combining axisymmetric, nonsymmetric, and hierarchical shape transformations. (**A**) A 22- by 22-cm membrane programmed to inflate into nonsymmetric and hierarchical stone shapes. Natural river stones with the same color encircle the membrane. The mesh design is shown on the bottom. (**B**) A membrane programmed to inflate into the shape of a *G. amethorum* plant. The leaves are arranged in a spiral around a center point and use suspended mesh supports to maintain the high-aspect-ratio mesh patterns. (**C**) Digital photograph of a *G. amethorum* plant. (**D**) The Gaussian curvatures of the inflated and deflated membranes. (**E**) A topographical map with stretchable electroluminescent display that inflated to the landscape's true 3D shape by use of CCOARSE. The black contour lines and color-coded regions represent areas of equal elevation.

membranes allow for locally concave 3D shapes, which is otherwise difficult to achieve pneumatically because the positive air pressure energetically prefers the convex conjugate shape. An nth-order mesh pattern in a hierarchical mesh pattern will inflate to a protruding shape on the $(n - 1)$–order parent. In the synthetic papillae shown in Fig. 3B, the first-order shape is a negative Gaussian curvature surface, and the second-order shapes are positive and zero Gaussian curvature surfaces. To achieve these complex architectures, we overlaid the second-order mesh designs onto the first-order mesh. We included a boundary mesh around the second-order mesh patterns when the second-order mesh design overlapped bare silicone in the first-order structure. To reduce the distortion on the first-order structure caused by the boundary mesh, we included serpentine segments that expanded upon inflation. Including higher-order structures in this manner rotated the uppermost region of the first-order structure by less than 7°.

An additional challenge occurred when the 2D membrane shape and mesh patterns were noncircular. Under the uniform loading of pneumatic inflation, the low bending modulus of a mesh mat causes a noncircular mesh strip to curve into a more circular shape. To prevent the mesh strips from bending, we again drew inspiration from the cephalopod, which uses horizontal muscle fibers to squeeze soft tissue into high-aspect-ratio papillae. To imitate this functionality, we added a simple additional step to our fabrication process, which included gluing (Sil-Poxy, Smooth-On) horizontal mesh supports to the underlying laser-cut patterns (Fig. 3C). The mesh supports were porous so as to allow airflow and, when the membrane was inflated, prevented the embedded mesh patterns from bending. Two inflated membranes with identical, elliptical mesh patterns are shown in Fig. 3C. The left pattern, without mesh supports, bent until the minor axis width increased from 16 to 23 mm; however, the right pattern, with suspended mesh supports, inflated to our desired shape profile. Collectively, the ability to create axisymmetric, nonsymmetric, and hierarchically complex morphologies demonstrates the versatility of our technique.

By combining these morphologies, we developed synthetic skins that imitate natural shapes and camouflage into their background environments. For example, an inflated membrane programmed to deform into nonsymmetric and hierarchical stone shapes is shown in Fig. 4A (movies S5 and S6). The membrane was surrounded by natural river stones so as to demonstrate the visual blending of the membrane into its rocky environment. We painted both the artificial and natural stones a warm gray in order to control for differences in coloration. The artificial stone shapes combined simple and compound papillae characteristics found in cephalopod camouflage motifs (*4*, *5*); to replicate this complexity, we programmed each stone with up to four axisymmetric, nonsymmetric, or hierarchical designs. Like cephalopod papillae, the artificial stones do not reproduce the exact shapes of surrounding stones but break up the flat membrane's square shape and add contrast from external lighting to avoid detection or recognition (*4*, *5*). The dramatic changes in Gaussian curvature from the deflated to inflated state are shown in Fig. 4D; the large variety of negative and positive Gaussian curvature surfaces were characteristic of natural stone.

In addition to the rounded stones, we programmed a membrane to imitate the high-aspect-ratio shape of the *Graptoveria amethorum* plant (Fig. 4B and movie S7), a succulent with leaves arranged in a spiral. To maintain the high-aspect-ratio deformation in the nonsymmetric leaves, we again applied suspended mesh supports to prevent circumferential expansion and direct inflation out of plane. We split the 3D leaf shapes into multiple 2D cross sections and programmed the silicone length fraction across each cross section so as to achieve the 3D shape control (Fig. 4C). Despite the larger and smaller leaves being pressurized by the same air source, each leaf inflates to its target shape because the CCOARSE mesh pattern restricts the local radial strain in each silicone segment to the same programmed $\varepsilon_{silicone}$. As shown in Fig. 4D, the Gaussian curvature of the inflated *G. amethorum* membrane had a regular arrangement of high-curvature surfaces.

We used CCOARSE to control the shape of a 3D electroluminescent display embedded on a topographical map (Fig. 4E and movie S8). Black contour lines and color-coded regions of equal elevation represent the 3D landscape on the 2D map. Inflating the map revealed the landscape's true 3D shape. We used CCOARSE to control the 3D topography and integrated a stretchable electroluminescent display in high-elevation regions for illumination (*36*).

We have shown that CCOARSE is a simple and scalable process for the prescriptive patterning of 2D surfaces that dynamically actuate into complex 3D shapes. By characterizing the anisotropic stretching of silicone-mesh composites, we were able to use curve fitting to program the shape change of these membranes, solving a long-standing design and control challenge. Cephalopod papillae morphology inspired our concentric mesh designs and hierarchical membrane structures, which enabled textural camouflage in a river stone environment. Although demonstrated here with pneumatically actuated elastomers, CCOARSE can be implemented with any pair of materials that have different stretching responses (such as swelling hydrogels or dielectric elastomer actuators) (*20*, *21*). Improvements in the maximum attainable strain or in the mesh patterning resolution would allow for higher-aspect-ratio shape transformations. Patterning materials with dynamic stiffness (for example, fluidic channels that could be selectively pressurized) would enable dynamic control of the shape curvature for 3D displays and vanishing human-machine interfaces with programmed pixels of texture (*36*, *37*). Additionally, accounting for circumferential and radial stress variations in hierarchal features would improve the accuracy of hierarchical shape reproduction.

REFERENCES AND NOTES

1. C. Darwin, F. Darwin, *The Power of Movement in Plants* (Appleton, 1897).
2. H. Liang, L. Mahadevan, *Proc. Natl. Acad. Sci. U.S.A.* **108**, 5516–5521 (2011).
3. J. Braam, *New Phytol.* **165**, 373–389 (2005).
4. J. J. Allen, G. R. Bell, A. M. Kuzirian, S. S. Velankar, R. T. Hanlon, *J. Morphol.* **275**, 371–390 (2014).
5. D. Panetta, K. Buresch, R. T. Hanlon, *Biol. Lett.* **13**, 20170070 (2017).
6. J. J. Allen, G. R. R. Bell, A. M. Kuzirian, R. T. Hanlon, *J. Morphol.* **274**, 645–656 (2013).
7. R. F. Shepherd *et al.*, *Proc. Natl. Acad. Sci. U.S.A.* **108**, 20400–20403 (2011).
8. R. V. Martinez *et al.*, *Adv. Mater.* **25**, 205–212 (2013).
9. D. Rus, M. T. Tolley, *Nature* **521**, 467–475 (2015).
10. D. Trivedi, C. D. Rahn, W. M. Kier, I. D. Walker, *Appl. Bionics Biomech.* **5**, 99–117 (2008).
11. M. Calisti *et al.*, *Bioinspir. Biomim.* **6**, 036002 (2011).
12. H. Thérien-Aubin, Z. L. Wu, Z. Nie, E. Kumacheva, *J. Am. Chem. Soc.* **135**, 4834–4839 (2013).
13. J. Kim, J. A. Hanna, M. Byun, C. D. Santangelo, R. C. Hayward, *Science* **335**, 1201–1205 (2012).
14. M. Ma, L. Guo, D. G. Anderson, R. Langer, *Science* **339**, 186–189 (2013).
15. C. Yu *et al.*, *Adv. Mater.* **25**, 1541–1546 (2013).
16. E. Wang, M. S. Desai, S.-W. Lee, *Nano Lett.* **13**, 2826–2830 (2013).
17. A. Lendlein, H. Jiang, O. Jünger, R. Langer, *Nature* **434**, 879–882 (2005).
18. Q. Ge *et al.*, *Sci. Rep.* **6**, 31110 (2016).
19. T. H. Ware, M. E. McConney, J. J. Wie, V. P. Tondiglia, T. J. White, *Science* **347**, 982–984 (2015).
20. R. Kempaiah, Z. Nie, *J. Mater. Chem. B Mater. Biol. Med.* **2**, 2357–2368 (2014).
21. Y. Liu, J. Genzer, M. D. Dickey, *Prog. Polym. Sci.* **52**, 79–106 (2016).
22. L. Phan *et al.*, *Chem. Mater.* **28**, 6804–6816 (2016).
23. S. Chatterjee, S. S. Velankar, *J. Intell. Mater. Syst. Struct.* **26**, 328–339 (2014).
24. B. Mosadegh *et al.*, *Adv. Funct. Mater.* **24**, 2163–2170 (2014).
25. M. Wehner *et al.*, *Soft Robotics* **1**, 263–274 (2014).
26. K.-J. Cho *et al.*, *Int. J. Precis. Eng. Manuf.* **10**, 171–181 (2009).
27. J. T. Overvelde *et al.*, *Nat. Commun.* **7**, 10929 (2016).
28. F. Ilievski, A. D. Mazzeo, R. F. Shepherd, X. Chen, G. M. Whitesides, *Angew. Chem.* **50**, 1890–1895 (2011).
29. M. A. McEvoy, N. Correll, *Science* **347**, 1261689 (2015).
30. S. Daynes, A. Grisdale, A. Seddon, R. Trask, *Smart Mater. Struct.* **23**, 012001 (2014).
31. S. Daynes, R. S. Trask, P. M. Weaver, *Smart Mater. Struct.* **23**, 125011 (2014).
32. R. S. McCurley, W. M. Kier, *Biol. Bull.* **188**, 197–209 (1995).
33. J. R. A. Taylor, W. M. Kier, *Science* **301**, 209–210 (2003).
34. W. H. Yang, W. W. Feng, *J. Appl. Mech.* **37**, 1002 (1970).
35. S. Fairman, C. S. Cutshall, *Mechanics of Materials* (Chapman & Hall, 1953).
36. C. Larson *et al.*, *Science* **351**, 1071–1074 (2016).
37. A. A. Stanley, K. Hata, A. M. Okamura, in *2016 IEEE International Conference on Robotics and Automation (ICRA)*. (2016), pp. 2718–2724.

ACKNOWLEDGMENTS

This work was funded by a grant from the Army Research Office, grant W911NF-16-1-0006. R.T.H. was supported by Air Force Office of Scientific Research grant FA9550-09-0346. We thank A. Rocha-Olivares for use of his photo of a *G. amethorum* plant.

SUPPLEMENTARY MATERIALS

www.sciencemag.org/content/358/6360/210/suppl/DC1
Materials and Methods
Supplementary Text
Figs. S1 to S4
Movies S1 to S8

2 May 2017; accepted 15 August 2017
10.1126/science.aan5627

Science

Stretchable surfaces with programmable 3D texture morphing for synthetic camouflaging skins

J. H. Pikul, S. Li, H. Bai, R. T. Hanlon, I. Cohen and R. F. Shepherd

Science **358** (6360), 210-214.
DOI: 10.1126/science.aan5627

3D texture morphing for camouflage

Some animals, such as cephalopods, use soft tissue to change shape reversibly for camouflage and object manipulation. Pikul *et al.* used fixed-length fiber mesh embedded in a silicone elastomer to transform a flat object into a 3D structure by inflating membranes (see the Perspective by Laschi). Painted models of rocks and plants were also created that could be morphed to fully blend into their surroundings.

Science, this issue p. 210; see also p. 169

Science (print ISSN 0036-8075; online ISSN 1095-9203) is published by the American Association for the Advancement of Science, 1200 New York Avenue NW, Washington, DC 20005. The title *Science* is a registered trademark of AAAS.